CHAPTER 3

Experimental and Computational details

3.1 Experimental details

3.1.1 Experimental setup

The schematic diagram of the experimental setup used for the present study has been illustrated in fig. 3.1. The flow of air is initiated by an air blower of 5.5kW capacity; speed of the blower is controlled by a three-phase variac. The flow from the blower passes through stabilizing channel so that the dynamic pressure is converted into static pressure. The stabilized air is passed through the heater, where the air comes in contact with the heating rods. The temperature of heated air is controlled by controlling the voltage with the help of signal phase variac. The heated air goes through the settling chamber where a honeycomb straightener of 500mm in length is placed to eliminate secondary mean velocity. The straighten flow passes through the reducer with a contraction ratio of 15:1 to get a uniform velocity and temperature profile at the exit of the nozzle. The size of the nozzle is $a = 20mm$ in height and $260mm$ in width to maintain an aspect ratio of 13:1. The setup is insulated with the asbestos strip up to the nozzle to minimise the heat loss, because these losses may influence the surrounding environment which will alter the temperature profile. The wavy wall is crafted on timber wood using a CNC machine. The flexible plywood of 7mm thickness is fixed over the wooden wavy pattern and it is smoothened by applying wood filler and once it is dry, the surface is scrubbed with sandpaper. Finally, the surface is spray painted with thermally stable matte black paint for high emissivity.

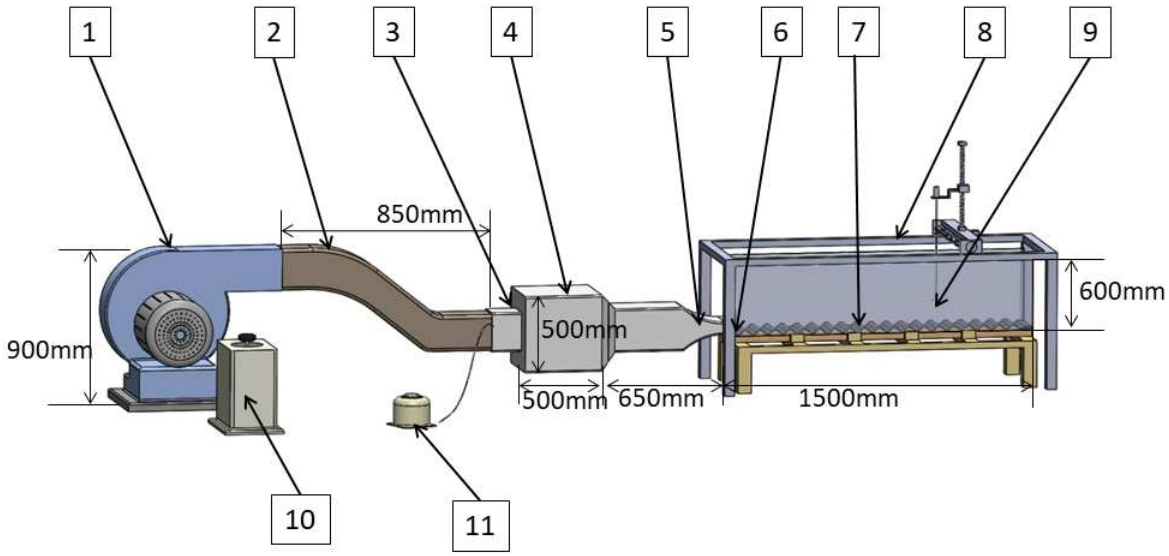

Figure 3.1: Experimental setup (1) Air blower, (2) Stabilizing channel, (3) Air heater, (4)Settling chamber with honeycomb straightener, (5) Reducer duct, (6) Nozzle, (7) Bottom wall, (8) Traversal mechanism, (9) Probe holder (10) Single phase variac for blower and (11) Single phase variac for air heater.

The thermal expansion and the thermal conductivity of the flexible plywood are very low, which makes plywood a perfect choice for the wall with an adiabatic condition. The width of the bottom wall is equal to the width of the nozzle and the length is taken as $75a$, in order to capture all the three zones of the flow adequately. The wavy wall is placed on a wooden frame. The test section is enclosed by an acrylic sheet of height $30a$ from both the sides to maintain the 2D nature of jet in most of the domain. The acrylic sheet is placed vertically above the nozzle to avoid any co-flow in the test section. The two dimensional transverse mechanism is used for mounting the thermocouple and hot wire anemometer to measure the temperature and velocity profiles within the flow domain. The probe can be moved 500mm in cross-stream and 1600mm in streamwise direction with the least count of 0.5mm. The uncertainty of the transverse mechanism is $\pm 0.5mm$ in both the directions. The base of transverse mechanism is made heavy by using solid bars of cast iron so that the vibration due to the movement of probe is minimized.

3.1.2 Methodology

A Dantec Dynamics constant temperature anemometer with a single sensor miniature wired probe has been used to measure the mean and turbulent velocities in the flow domain. The sensor has a diameter of $5\mu m$ and length $1.25mm$. The probe is calibrated us-

ing the 4th order polynomial curve for 15 different known velocities in the range of 0.5m/s to 35m/s. The probe is calibrated in a separate arrangement. The sampling rate is kept at 10kHz and the number of samples is 200000 using 12-bit A/D board, i.e. time taken for reading at each point is 20 seconds. The different sampling rates from 5kHz to 12 kHz have been tasted and found that beyond 8kHz the mean velocity error remains within 1% at different downstream locations. Therefore, a sampling rate of 10kHz has been chosen. In the literature [36, 43, 65], the sampling rate is kept around 10kHz for the velocity measurement of the turbulent jet by Dantec Dynamics hotwire anemometer. The different sampling periods are also tested between 10s and 30s for 10kHz frequency and it is found that 20s is sufficient, indicating that the difference is almost insignificant for higher sampling period. For this sampling rate and number of samples, the uncertainty of the mean and fluctuating velocities is less than 1.5% and 4% respectively. The uncertainties are calculated as mentioned by Aberneth et al. [2]. The probe is fixed on the manual traverse mechanism which can move 500mm in the cross-stream direction and 1600mm in the streamwise direction with a least count of 0.5 mm. The velocity has been measured from 0.2 onwards at the crest and 0.2+2A onwards at the trough in the wall normal direction from the wall due to the thickness of probe holder, where "a" is nozzle height and "A" is the wavy wall amplitude. For the mean and fluctuating temperature measurements in the flow field, a K-type thermocouple of diameter 0.1mm is used. A round bead has been made by joining two thermocouple wires and the diameter of the bead is 0.25mm. The schematic diagram of probe is shown in figure 3.2, where the diameter of probe is kept 1mm in lower portion so that the flow does not get disturbed during the measurement. The thermocouple probe holder diameter is 1mm up to a distance of 300mm; above 300mm, to increase the stiffness of the probe, the diameter is increased to 5mm as this portion does not interfere the flow region of our interest. At the top, the probe holder is of 30mm diameter so that it can be mounted on the traverse mechanism. The NI 9213 data acquisition (DAQ) system is used to record the data on the computer. A different set of frequencies and number of samples have been tested, and frequency of 200Hz and 6000 samples are selected for the final measurement. For this frequency and number of samples, the uncertainty in the mean and fluctuating temperatures is less than 0.87% and 2%, respectively. To capture the bottom wall temperature, FLIR-E75 infrared camera is used. The FLIR camera gives the best accuracy when mounted 1 m away and is normal to the surface. The FLIR camera is mounted on the wooden frame, placed over the transverse mechanism frame and the distance from the wall is kept 1m. The selected range of temperature measurement is -20^0C to 120^0C for capturing the image and the resolution of FLIR is 0.1^0C.

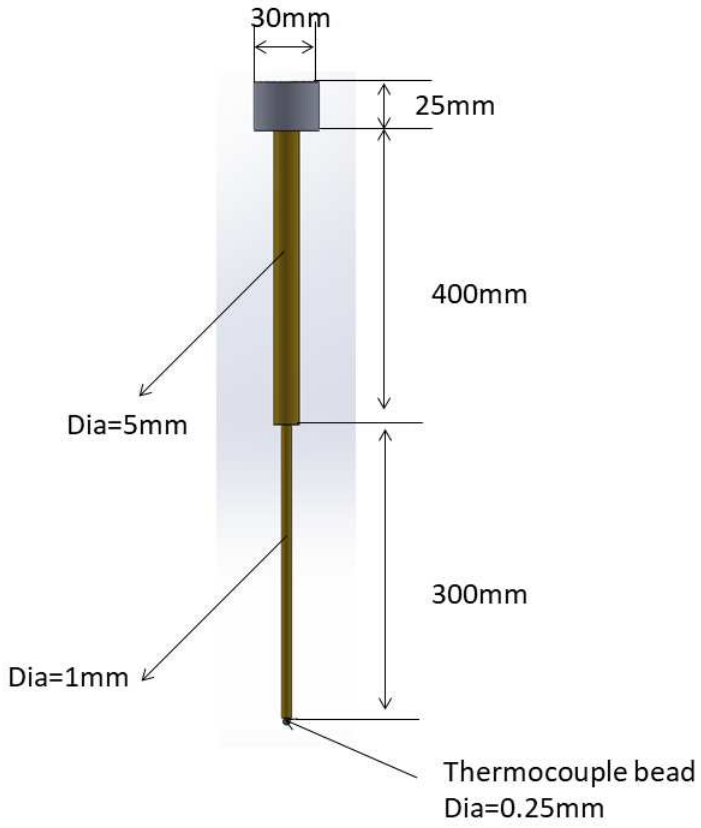

Figure 3.2: The schematic of thermocouple probe

3.1.3 Uncertainty analysis

In the experimental work, the errors can be described as bias errors and random errors. The bias error is the average of the difference between the estimated value by the measuring equipment and the actual value. The bias error remains constant for different set of readings. The proper calibration of the measuring probe can control the bias error. Random errors come into existence due to uncontrolled factors which affect the experimental results. The fluctuation in voltage supply, the movement of ambient fluid, and human error in the proper positioning of the probe are essential factors in the present experiment, which will give rise to the random errors. The random error is calculated by performing n number of runs for the same conditions at different point of time. The random error is calculated by using the equation as mentioned by Aberneth et al. [2].

$$S = \left[\sum_{i=1}^{n} (x_i - \overline{x})^2/(n-1)\right]^{1/2} \tag{3.1}$$

$$S_x = S/\sqrt{n} \tag{3.2}$$

Where n is the number of samples, $\overline{x}$ is the mean value, and S is the calculated random factor index. The calculated uncertainty for mean velocity and fluctuating velocity is less than 1.5% and 4% respectively for hot wire anemometer. The uncertainty in the mean and fluctuating temperatures of thermocouple is less than 0.87% and 2%, respectively. The uncertainty in the bottom wall temperature, given by FLIR camera, remains below 1.5%. The uncertainty in the Reynolds number at the inlet has been calculated by $\triangle Re - \pm\sqrt{((\partial Re/\partial u) * \triangle u)^2 + ((\partial Re/\partial h) * \triangle h)^2}$, as mentioned by Kline and McCintock [52], where $\triangle Re$ is the maximum uncertainty in the Reynolds number at the inlet. The uncertainties in the setup and the measured parameters are listed in table. . To check the reliability of results obtained from the experimental setup, the streamwise mean velocity and the turbulent intensity profile with error bar have been shown in fig. 3.3 . The streamwise mean velocity and turbulent intensity are plotted for the wavy wall with amplitudes 0.2, 0.4, and 0.6 and the plane wall, at a location X = 31.875. For the error estimation, readings are repeated five times for all the cases. The error is within 1.5% and 4% for the mean velocity and turbulent intensity profiles, respectively.

Table 3.1: The maximum uncertainties of basic parameters.

Parameters	uncertainty
Height of nozzle	$0.5mm$
transverse mechanism movement in x-direction	$0.5mm$
transverse mechanism movement in y-direction	$0.5mm$
mean streamwise velocity	1.5%
fluctuating streamwise velocity	4%
Reynolds number	2.9%
mean flow temperature	0.87%
fluctuating flow temperature	2%
wall temperature (FLIR camera)	1.5%

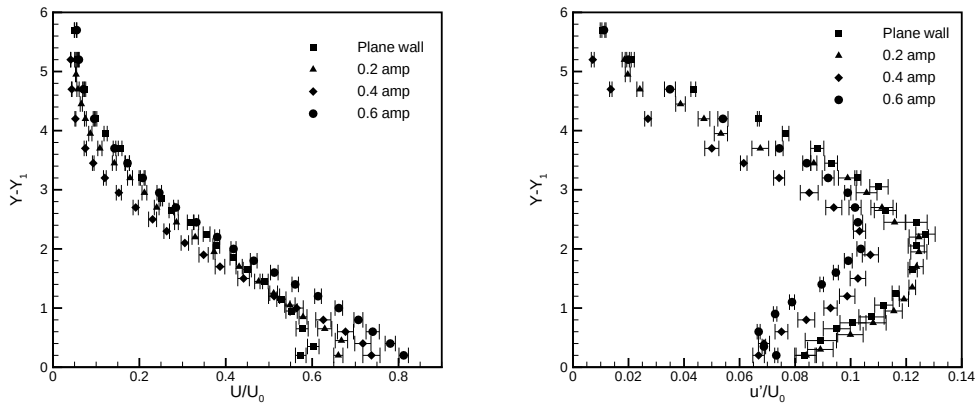

(a) (b)

Figure 3.3: The variation of streamwise (a) mean velocity and (b) turbulent intensity in cross stream direction at $X = 31.875$

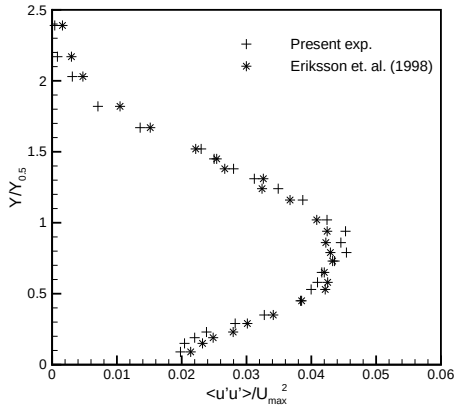

Figure 3.4: Variation of $< u'u' >$ in cross stream direction at location X=40

3.1.4 Setup Validation

The present setup is validated for the fluid flow characteristics of an unheated jet with the experimental results of Eriksson et al. [25]. Eriksson et al. [25] have performed the experiment for a Reynolds number of 9600 at the exit of the nozzle for a plane wall jet. The inlet condition is kept same as that of Eriksson et al. [25] in the present arrangement. In fig. 3.4, the X normal Reynolds stress profile of present result is compared with the result of Eriksson et al. [25] at X=40. The present experimental result matches very well with the result of Eriksson et al. [25]. A maximum difference of 7% is observed in the present result. The thermal characteristics of the present setup is validated with the experimental data of Holland and Liburdy [41] for the plane wall jet. The present experimental setup is run with the same inlet conditions as used in Holland and Liburdy [41]. Fig. 3.5 shows the comparison of present experimental result with the result of Holland and Liburdy [41] for the temperature profile in wall normal direction at the locations $X = 10.4$, $X = 15.4$ and $X = 20.3$. The present result matches very well with the literature result for all the three locations. In the case of bottom wall temperature, the present result gives a good agreement with the result of Holland and Liburdy [41] in the near flow field till $X = 18.75$, as shown in fig. 3.6 . The present result gets little deviated from the literature result as fluid moves further, with a maximum difference of 6.8%. The difference in the results might be due to the methodology used, as in present case FLIR camera has been used for the bottom wall surface temperature whereas thermocouples were embedded on the wall in the case of Holland and Liburdy [41].

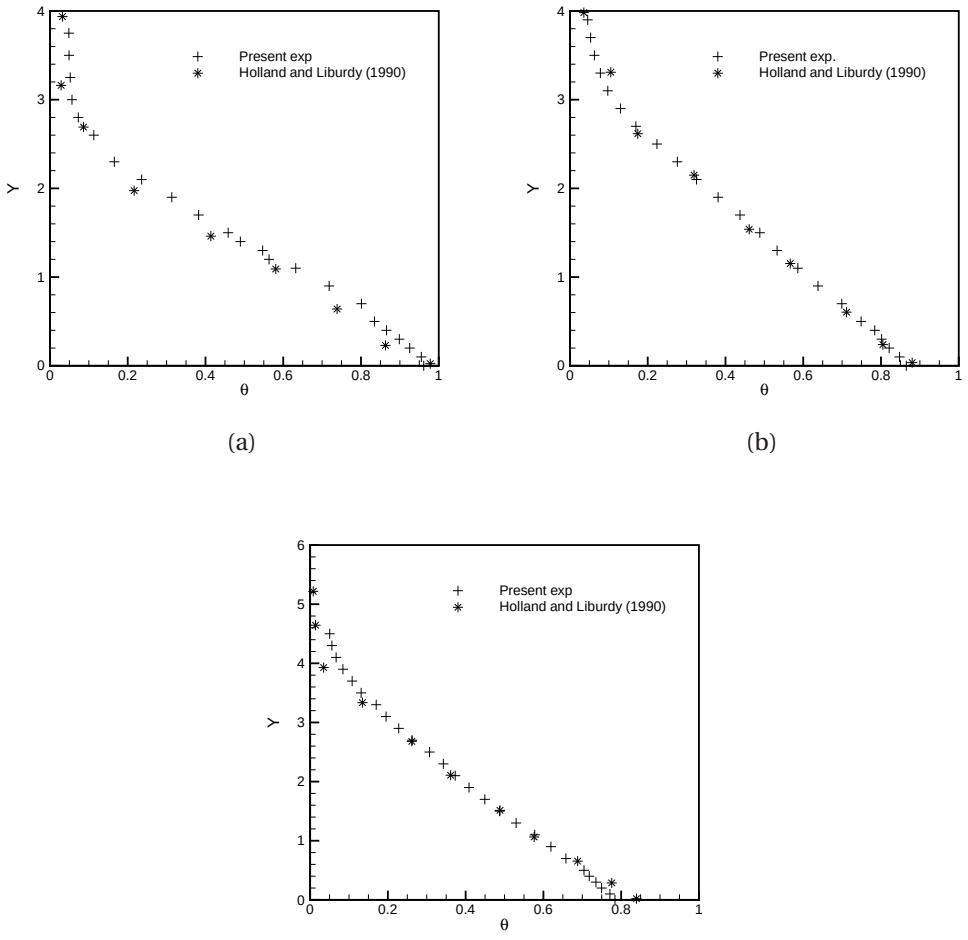

Figure 3.5: Temperature profile in wall normal direction at location (a) $X = 10.4$, (b) $X = 15.4$ and (c) $X = 20.3$

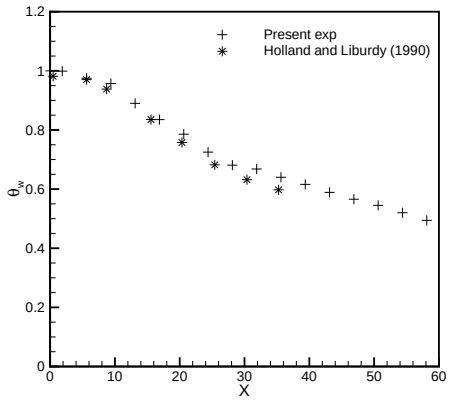

Figure 3.6: The variation of bottom wall temprature for plane wall jet

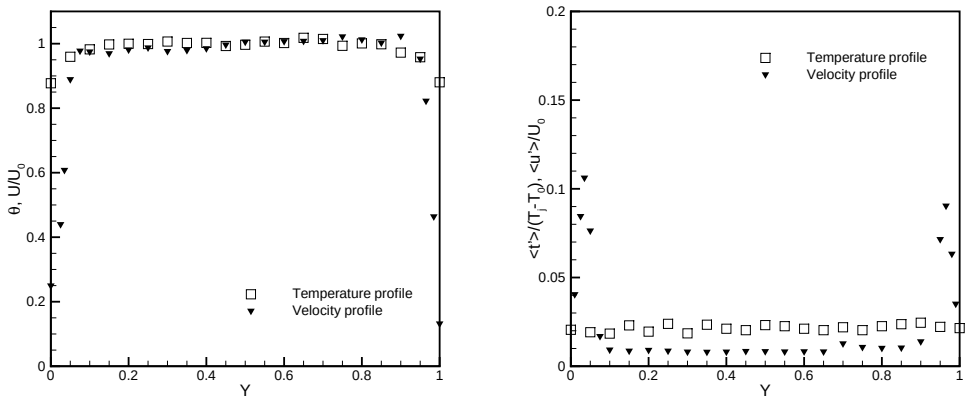

(a) (b)

Figure 3.7: (a)The mean temperature and velocity profiles at the inlet ($X = 0.25$) and (b) The fluctuating temperature and velocity profiles at the inlet ($X = 0.25$)

3.1.5 Inlet conditions

The experiment has been conducted for the Reynolds number of 15000. To achieve this, velocity of 10.95 m/s is maintained at the exit of the nozzle. The jet is heated 30 ^0C above the ambient temperature. The mean velocity and the mean temperature profiles near the inlet $X = 0.25$ are plotted in fig. 3.7a. The uniform top hat profile can be seen for both the velocity and the temperature profiles similar to the inlet profile of Sun and Ewing [95] and Deo et al. [23]. The variation of 4% and 3.3% is noticed for the mean velocity and temperature profiles in the central region, $0.1a$ away from the nozzle top and bottom edges. The profiles of fluctuating velocity and temperature near the inlet are illustrated in fig. 3.7b. The fluctuating velocity at the exit is around 1% and it goes up to 10.6% in the inner shear layer near the wall and 9% in the outer shear layer where jet comes in contact with the ambient. In the case of temperature, the fluctuation remains the same throughout the nozzle height, which is around 2% of the $(t_0 - t_\infty)$.

3.2 Computational details

3.2.1 Governing equations

The study of turbulent flow field is done by solving the Reynolds averaged Navier-Stokes (RANS) equations. The flow is assumed to be steady, incompressible, and 2-D in nature. Air is considered as the working fluid whose thermophysical properties are assumed to

be constant. The flow condition at the exit of the nozzle is considered as fully turbulent and unidirectional (along x-axis). The normalized continuity, momentum, and energy equations for the incompressible flow are mentioned below.

The inlet velocity U_0 is used to normalize the velocity. The nozzle height a is used to normalize the length and the temperature difference $T_j - T_\infty$ is used to normalize the temperature.

.

$$U_i = \frac{\bar{u}_i}{U_0}, \qquad X_i = \frac{\bar{x}_i}{a}, \qquad \theta = \frac{\overline{T} - T_\infty}{\overline{T}_j - T_\infty}, \qquad P = \frac{\bar{p} - \bar{p}_0}{\rho U_0^2}$$

$$k_n = \frac{k}{U_0^2}, \qquad \varepsilon_n = \frac{\varepsilon}{U_0^3/a}, \qquad \alpha_n = \frac{\alpha_t}{\alpha}, \qquad \nu_{t,n} = \frac{\nu_t}{\nu}$$

.

$$\frac{\partial U_i}{\partial X_i} = 0 \tag{3.3}$$

$$U_j \frac{\partial U_i}{\partial X_j} = -\frac{\partial (P + 2/3 * k_n)}{\partial X_i} + \frac{1}{Re} \frac{\partial}{\partial X_j} [(1 + \nu_n)(\frac{\partial U_i}{\partial X_j} + \frac{\partial U_j}{\partial X_i})] \tag{3.4}$$

$$U_j \frac{\partial \theta}{\partial X_j} = \frac{1}{RePr} \frac{\partial}{\partial X_j} [(1 + \alpha_n) \frac{\partial \theta}{\partial X_j}] \tag{3.5}$$

3.2.1.1 $k - \varepsilon$ RNG model

The turbulent quantities k and ε have been solved using the turbulent RNG $k - \varepsilon$ model. This model is introduced by Yakhot and Orszag [107] which works on the renormalization group theory.

Turbulent Kinetic energy equation (k_n)

$$U_j \frac{\partial k_n}{\partial X_j} = \frac{1}{Re} \frac{\partial}{\partial X_j} [(1 + \frac{\nu_{t,n}}{\sigma_k}) \frac{\partial k_n}{\partial X_j}] + G_n - \epsilon_n - D_n \tag{3.6}$$

Kinetic energy generation

$$G_n = \frac{\nu_{t,n}}{Re}[(\frac{\partial U_i}{\partial X_j} + \frac{\partial U_j}{\partial X_i})]\frac{\partial U_i}{\partial X_j} \tag{3.7}$$

The magnitude of the strain rate tensor

$$S = \sqrt{2\bar{S_{ij}}\bar{S_{ij}}} \tag{3.8}$$

The differential equation for turbulent viscosity

$$d(\rho^2 k/\sqrt{\varepsilon\mu}) \quad = \quad 1.72(\hat{\nu}/\sqrt{\hat{\nu}^3 - 1 + C_\nu})d\hat{\nu} \tag{3.9}$$

$$\hat{\nu} \quad = \quad \mu_{eff}/\mu$$

$$C_\nu \quad \approx \quad 100$$

Turbulent viscosity

$$\nu_{t,n} = C_\mu Re\frac{k_n^2}{\epsilon_n} \tag{3.10}$$

Dissipation energy equation

$$U_j\frac{\partial \epsilon_n}{\partial X_j} = \frac{1}{Re}\frac{\partial}{\partial X_j}[(1 + \frac{\nu_{t,n}}{\sigma_\epsilon})\frac{\partial \epsilon_n}{\partial X_j}] + C_{1\epsilon}\frac{\epsilon_n}{k_n} - C_{2\epsilon}^*\frac{\epsilon_n^2}{k_n} \tag{3.11}$$

where

$$C_{2\epsilon}^{*} = C_{2\epsilon} + \frac{C_{\mu}\eta^{3}(1-\frac{\eta}{\eta_0})}{1+\beta\eta^{3}}$$

$$\eta = \frac{Sk_n}{\epsilon_n}$$

The values of constants are $C_{1\epsilon}$=1.42, $C_{2\epsilon}$=1.68, η_0=4.38, β = 0.012, σ_k=0.7194, C_{μ} = 0.0845 and σ_{ϵ}=0.7194.

The differential equation for turbulent viscosity eq. 3.9 is integrated to get the precise information of the effective turbulent transport variation with the effective Reynolds number which makes the RNG model more compatible for the viscous sub layer (low Reynolds number). In the high Re limits, eq. 3.9 reduces to eq. 3.10.

3.2.1.2 $k-\omega$ SST model

SST k-ωmodel: This model is a upgraded version of standard $k-\omega$ turbulence model.

Turbulent Kinetic energy

$$U_j\frac{\partial k_n}{\partial X_j} = \frac{1}{Re}[(1+\frac{\nu_{t,n}}{\sigma_k})\frac{\partial k_n}{\partial X_j}] + \min(G_n, 10\beta^{*}\kappa_n\omega_n) - \beta^{*}k_n\omega_n \tag{3.12}$$

Dissipation Rate

$$U_j\frac{\partial \omega_n}{\partial X_j} = \frac{1}{Re}\frac{\partial}{\partial X_j}[(1+\sigma_{\omega}\nu_{t,n})\frac{\partial \omega_n}{\partial X_i}] + \alpha\frac{Re}{\nu_t}\min(G_n, 10\beta\kappa_n\omega_n) - \beta\omega_n^2 \quad +2(1-F_1)\frac{\sigma_{\omega 2}}{\omega_n}\frac{\partial k_n}{\partial X_j}\frac{\partial \omega_n}{\partial X_j} \tag{3.13}$$

blending function

$$F_1 = tanh[\{\min(\quad \zeta, \eta)\}^4] \tag{3.14}$$

$$\zeta = \max(\frac{\sqrt{k_n}}{\beta^{*}\omega_n d}, \frac{500}{Red^2\omega_n}) \tag{3.15}$$

$$\eta = \frac{4\sigma_{\omega 2}\frac{k_n}{d^2}}{\max(2\sigma_{\omega 2}\frac{1}{\omega_n}\frac{\partial k_n}{\partial X_j}\frac{\partial \omega_n}{\partial X_j}, 10^{-10})} \tag{3.16}$$

$$\nu_{t,n} = Re\min[\frac{\kappa_n}{\omega_n}, \frac{a_1\kappa_n}{F_2\sqrt{\frac{\partial U_i}{\partial X_j}(\frac{\partial U_i}{\partial X_j}+\frac{\partial U_j}{\partial X_i})}}] \tag{3.17}$$

where

$$\sigma_k = \frac{1}{\frac{F_1}{\sigma_{k1}} + (\frac{1-F_1}{\sigma_{k2}})} \tag{3.18}$$

$$F_2 = tanh[\{\max(\frac{2\sqrt{k_n}}{\beta^*\omega_n d}, \frac{500}{Red^2\omega_n})\}^2] \tag{3.19}$$

The model constant are:

$a_1 = 0.31, \beta^* = 0.09, \alpha_1 = \frac{5}{9}, \alpha_2 = 0.44, \beta_1 = 0.075, \sigma_{k1} = 0.85, \sigma_{k2} = 1, \sigma_{\omega 1} = 0.5, \sigma_{\omega 2} = 0.856$

$$\alpha = \alpha_1 F_1 + \alpha_2(1-F_1)$$

$$\beta = \beta_1 F_1 + \beta_2(1-F_1)$$

$$\sigma_k = \sigma_{k1} F_1 + \sigma_{k2}(1-F_1)$$

$$\alpha_\omega = \sigma_{\omega 1} F_1 + \sigma_{\omega 2}(1-F_1)$$

The averaging of momentum and energy equations through Boussinesq approximation produces the Reynolds stress tensor and the turbulent heat flux, respectively. The Reynolds stress depends on the mean velocity gradient and the turbulent viscosity ν_t as

$$-\overline{u_i' u_j'} = \nu_t(\partial u_i/\partial x_j + \partial u_j/\partial x_i) - 2/3(k\delta_{ij}) \tag{3.20}$$

Where δ_{ij} is the Kronecker delta, whose value is 1 if $i = j$, otherwise its value is 0.

The turbulent heat flux depends on the turbulent viscosity ν_t, turbulent Prandtl number Pr_t and the temperature gradient. The turbulent Prandtl number is assumed to be constant; for air Pr_t= 0.7179. The turbulent heat flux is given as

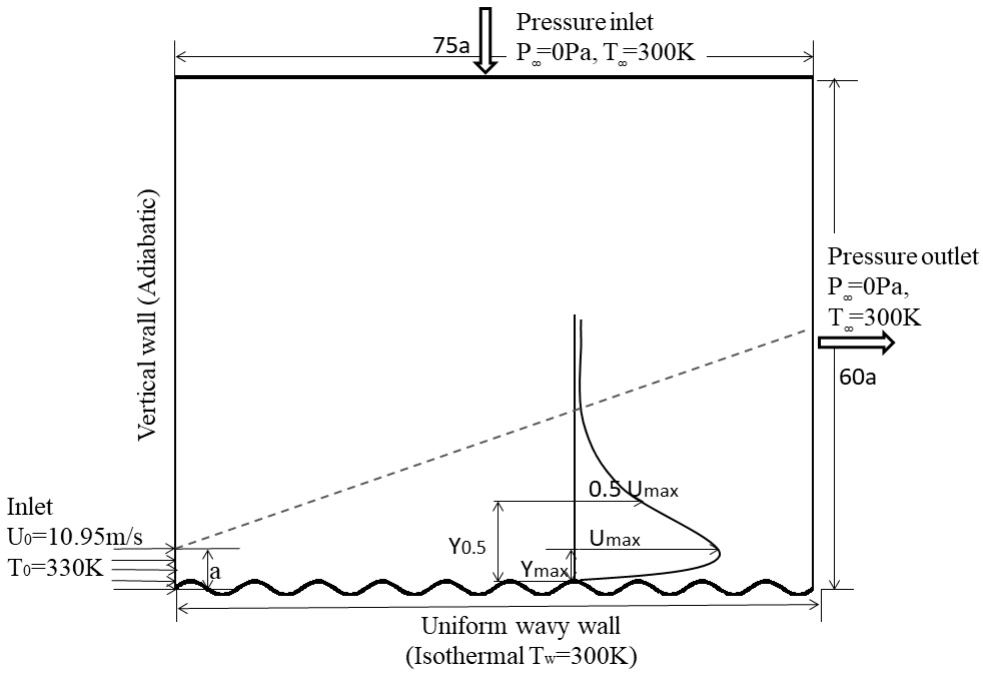

Figure 3.8: Schematic diagram for the computational domain of a turbulent wall jet flowing over a wavy wall

$$\overline{u_j' t'} = \nu_t / Pr_t (\partial T / \partial x_j) \tag{3.21}$$

3.2.2 Computational domain

The computational domain for different objectives of present research are discussed in this section.

3.2.2.1 Isothermal wavy wall

The computational domain for turbulent wall jet with a uniform wavy wall is illustrated in fig. 3.8. A slotted nozzle of height $a = 20mm$ has been used for the study of the jet on a sinusoidal wavy surface. The computational domain is set to be of 75a in length in the streamwise direction and 60a in length in the cross-stream direction in order to capture the flow field and heat transfer characteristics in the most effective manner. The domain size is taken as 75a along the x direction so that all the three zones (potential core, transition zone and develop zone) can be captured, and flow has enough space for the developed region. In the y-direction, the domain size is kept as 60a to maintain the quiescent

condition (no co flow) and to allow the free spread of jet in the wall-normal direction. The sinusoidal profile ($y = A * sin(\omega_N x)$) is used for the wavy wall, where $\omega_N = 2\pi N/L$ is the frequency with suffix N denoting the number of cycles for the given length L and A is the amplitude. The normalized amplitude A is obtained by dividing amplitude with the nozzle height 'a'. The amplitude A is varied from 0 to 0.8 and ω_N is changed from ω_4 to ω_{12}, to find out the optimum amplitude and frequency for which the heat transfer rate is maximum. At the inlet, the jet is heated to a temperature of 330K and a uniform velocity of 10.95m/s is maintained to get Reynolds number of 15000 which remains the same for all the cases. The bottom wall is at a constant temperature of 300K, same as the surrounding temperature.

3.2.2.2 Isothermal modified wavy wall

Fig. 3.9 shows the computational domain for a turbulent wall jet flowing over a modified wavy wall. In fig. 3.9a, the bottom wall is made partially wavy and partially plane. The partial wall is created by giving a segment of wall a wavy pattern from the leading edge followed by the plane wall; the wavy wall segment varies from 10% to 100% of the wall. The sinusoidal wavy wall has been used with formula ($y = A * sin(\omega_{10} x)$), where the frequency is fixed to ω_{10} and x is changed from 7.5a to 75a to get 10% (1 cycle) to 100% (10 cycles) wavy wall portion respectively. The amplitude of wavy surface has also been varied from 0.2 to 0.8. The computational domain with 40% wavy wall has been explained through fig.3.9a where 40% of the wall from the leading edge is in wavy pattern and the remaining 60% of wall is plane. Other parameters like nozzle height and the size of the domain remain same as the computational domain of the wavy wall. The second case of modified wavy wall is shown in Fig. 3.9b, partially linearly decaying (LD) wavy wall is used. For this, a segment of wall from the leading edge is made with constant amplitude 0.8, followed by the segment of linearly decaying wavy wall. In the region of LD wavy wall, the amplitude of wavy wall varied linearly from 0.8 amplitude to 0 in the downstream direction. The LD wavy wall segment varies from 100% to 0%. In case of 100 % LD wavy wall, the whole wall is made of linearly decaying amplitude, whereas in the case of 0%, the whole wall is made wavy with a constant 0.8 amplitude. The equation used for different cases is listed in table. 3.2, where 'n' represents number of cycle with constant amplitude. The $n = 1$ for 90% LD wavy wall, $n = 2$ for 80% LD wavy wall and so on till $n = 9$ for 10% LD wavy wall. Other parameters, like nozzle height and the size of domain remain same as the computational domain of the wavy wall.

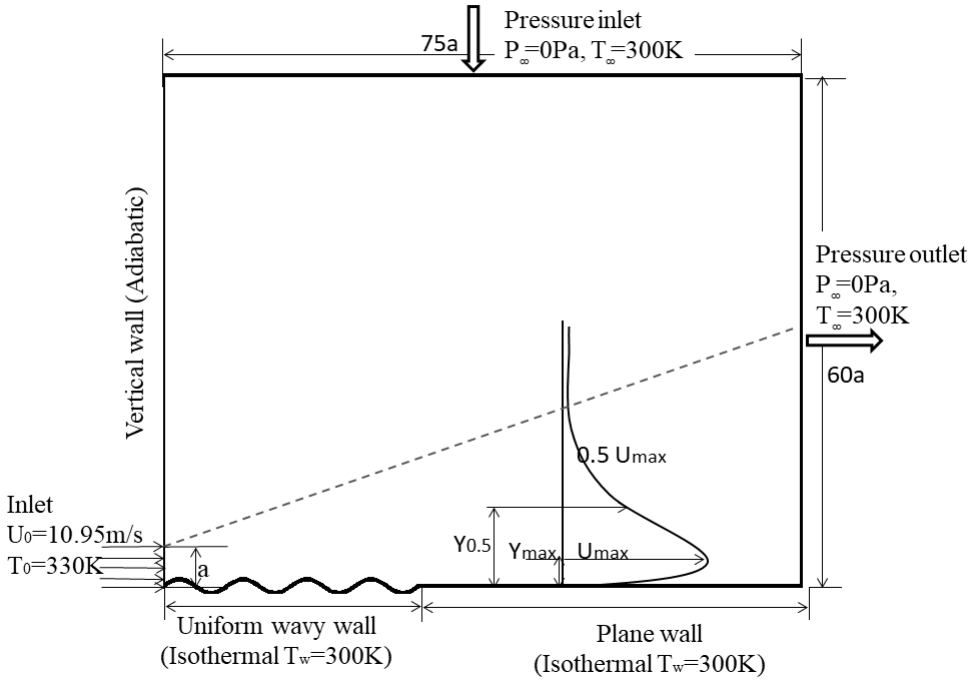

(a)

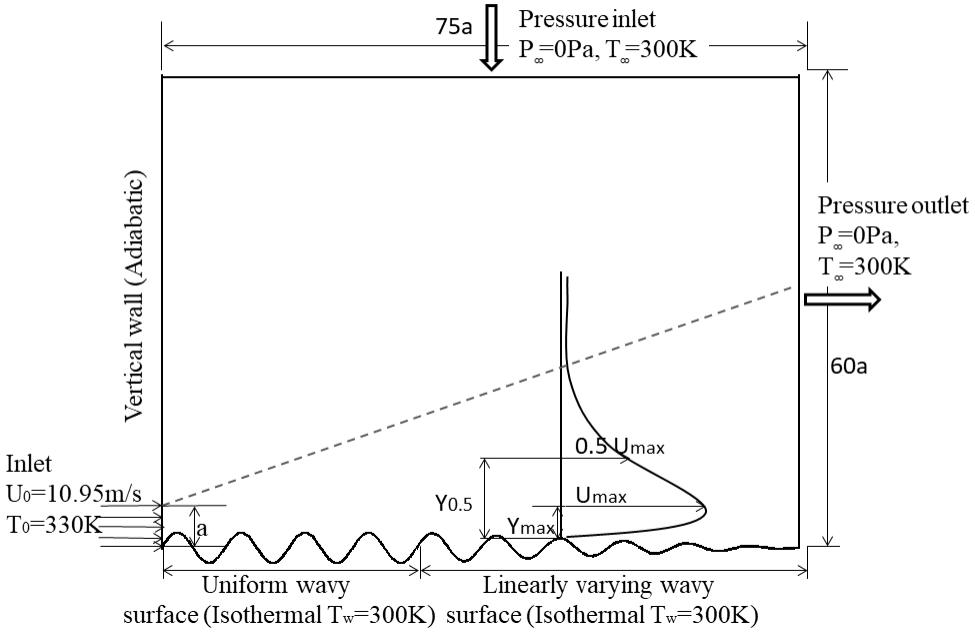

(b)

Figure 3.9: Schematic diagram for the computational domain of a turbulent wall jet flowing over a (a) partial wavy wall and (b) partially decaying wavy wall.

Table 3.2: The equations for the partially linearly decaying wavy wall

case	n	$y = f(x)sin(\omega x)$	Range of equation
100% LD	0	$f(x) = A(1-(x/L))$	$0 \le x \le L$
90%	1 to 9	$f(x) = A$	$0 \le x \le n(L/N)$
to 10% LD		$f(x) = \frac{A}{(N/n-1)}(N/n-(Nx/nL))$	$n(L/N) \le x \le L$
0% LD	10	$f(x) = A$	$0 \le x \le L$

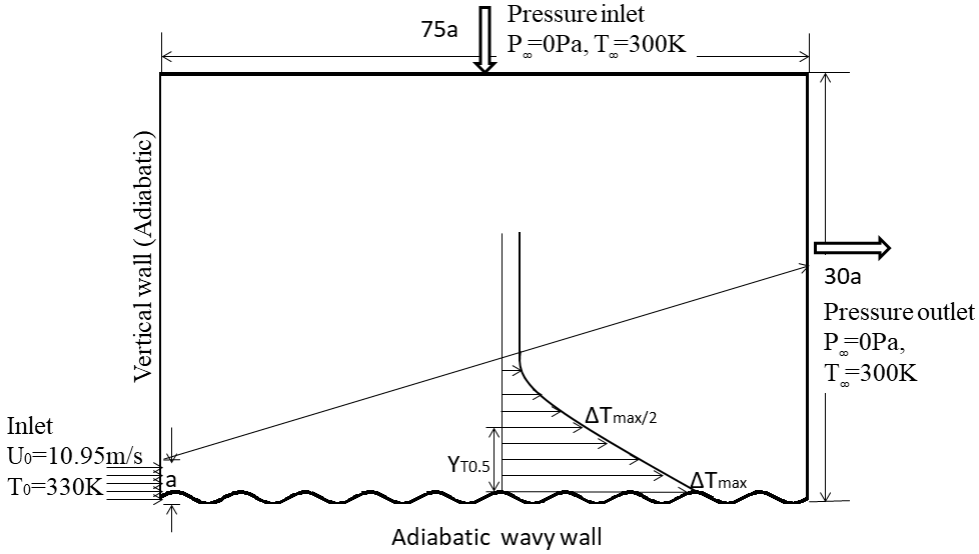

Figure 3.10: Schematic diagram for the computational domain similar to the experimental flow domain

3.2.2.3 Adiabatic wavy wall

Fig. 3.10 shows the computational domain to mimic the experimental flow domain. In order to do so, the bottom wall is made wavy throughout and maintained in an adiabatic condition. For different cases, the amplitude is changed from 0.0 to 0.6 and frequency remains the same, i.e., ω_{10} for all the cases. The height of the nozzle is a=20mm, the computational domain size is set to 75a in the streamwise direction and 30a in the cross-stream direction similar to the experimental flow domain.

3.2.3 Numerical approach and Boundary conditions

All the computational work have been done on a structured grid by using FLUENT. For pressure velocity coupling, SIMPLE (Semi Implicit Pressure Linked Equation) algorithm is used. All the convective terms and diffusive terms are discretized by using second order

upwind and second order central difference schemes respectively. The convergence of the solution is said to be obtained when the normalized residual of all the discretized variables other than the energy equation is lower than $10^{-4}$and for the energy equation it is set as 10^{-6}. Further increase in the residual value does not have any practical influence on the final outcomes.

The details of boundary conditions for the isothermal uniform wavy wall and modified wavy wall (partial wavy wall and partially linearly decaying wavy wall) are mentioned below:

Inlet:$U_0 = 10.95$m/s, $V_0 = 0$, $T_0 = 330K$, $k_n = 3/2\,(IU_0)^2$, $\epsilon_n = (C_\mu^{3/4} k^{1/2})/l$, and $\omega_n = k^{1/2}/C_\mu^{1/4}$, turbulent intensity$I$ is taken as 5% and turbulent length scale l is taken as $0.07a$ [17]

Bottom wall: No slip isothermal boundary condition,$U_0 = 0$, $V_0 = 0$, $T_w = 300K$, $k_n = 0$, $\epsilon_n = 0$, and $\omega_n = 0$

vertical wall: No slip adiabatic boundary condition,$U_0 = 0$, $V_0 = 0$, $\partial T/\partial N = 0$, $T_w = 300K$, $k_n = 0$, $\epsilon_n = 0$, and $\omega_n = 0$

Top edge: Pressure inlet, $P_\infty = 0$, $T_\infty = 300K$, $\partial U/\partial N = 0$, $\partial V/\partial N = 0$, $\partial k_n/\partial N = 0$, $\partial \epsilon_n/\partial N = 0$ and $\partial \omega_n/\partial N = 0$

Right side vertical edge: Pressure outlet,$P_\infty = 0$, $T_\infty = 300K$, $\partial U/\partial N = 0$, $\partial V/\partial N = 0$, $\partial k_n/\partial N = 0$, $\partial \epsilon_n/\partial N = 0$ and $\partial \omega_n/\partial N = 0$

The boundary condition for the adiabatic wavy wall, to mimic the experimental condition will remain same as the boundary condition of isothermal wavy wall at all the boundaries, except at the bottom wall.

Bottom wall: No slip adiabatic boundary condition,$U_0 = 0$, $V_0 = 0$, $\partial T/\partial N = 0$, $k_n = 0$, $\epsilon_n = 0$, and $\omega_n = 0$

3.2.4 Grid distribution

Fig. 3.11a shows a typical grid distribution for the two-dimensional computational domain. In fig. 3.11a, the nonuniform quadrilateral grids are used in the x and y directions to create the dense grids near the large gradients. To capture viscous boundary layer more effectively, the grid points are laid near the wall in such a way that $y^+ < 1$ and $x^+ < 1$. Grids in the cross-stream direction (y direction) is more dense near the wall. A total of 240 grids is distributed in the cross-stream direction, out of which 60 grids are distributed from the bottom wall to the height of the nozzle with an expansion ratio of 1.08 and remaining grids are distributed in the rest of the domain with an expansion ratio of 1.013. In the streamwise direction (x direction), the grids are fine near the exit of the nozzle by distributing

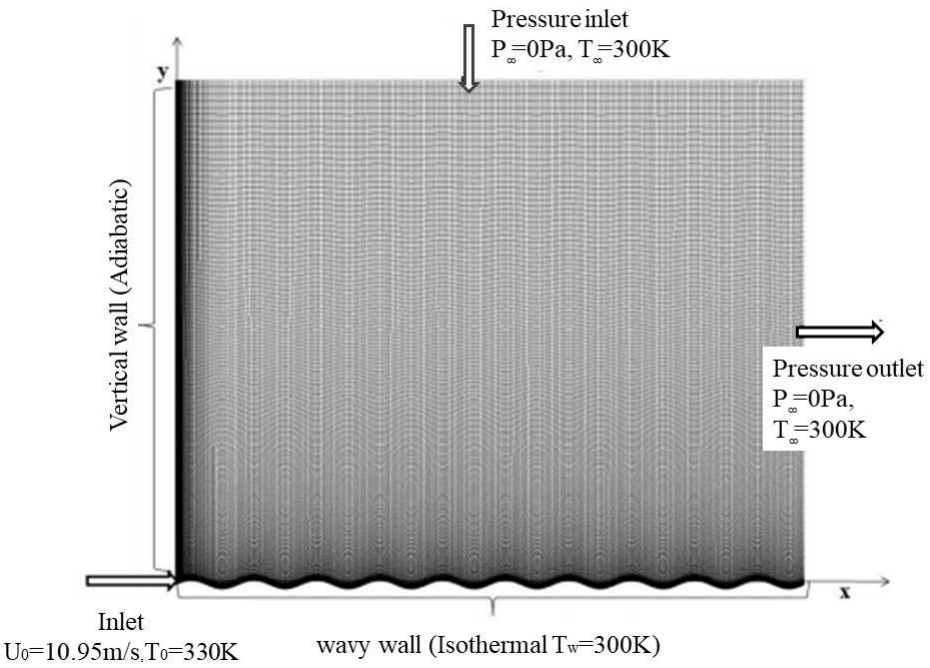

(a)

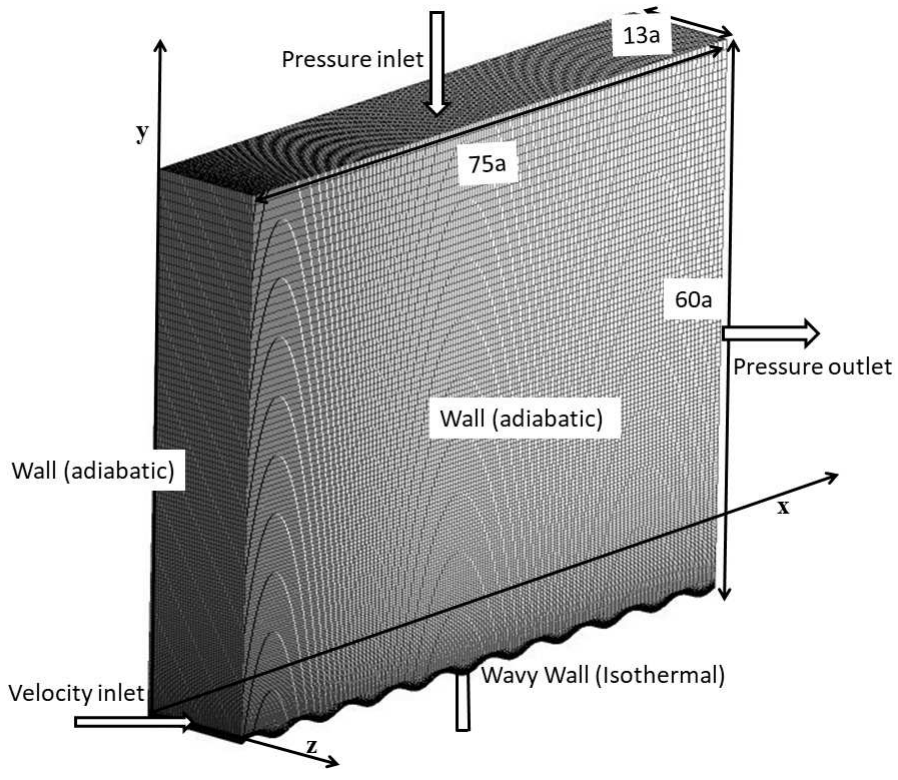

(b)

Figure 3.11: (a) 2D and (b) 3D grid distribution for the computation domain

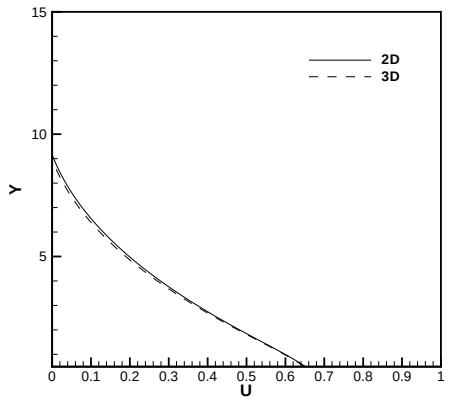

Figure 3.12: Comparison of streamwise mean velocity profile of 2D and 3D simulations

70 grids in the near flow field $X = 4$ with the expansion ratio of 1.073 and 260 grids are distributed uniformly in rest of the domain.

The problem is considered to be two-dimensional in nature. This two dimensional approximation is used by Assoudi et al. [9] and Kumar [53] for the investigation of duel jet. Kechiche et al. [50] and Azim [12] have also used this approximation for the plane wall jet. Under 2D approximation, the velocity in z direction remains zero throughout the domain. Before proceeding with this assumption, it is made sure that the three-dimensional problem also gives the similar result. In doing so, the aspect ratio of nozzle is kept as 13 which is sufficiently large. The 3D grid distribution for the present problem is shown in fig. 3.11b. For 3D simulation, slip wall boundary condition has been applied to the walls in the Z plane. Other boundary conditions are kept same as in the 2D computational domain. Holland and Liburdy [41], Song et al [93] and AbdulNour et al. [1] have used nozzle of aspect ratio 15, 12 and 17.8 respectively in order to have two dimensional flow structure. In order to check the authenticity of 2D flow field, the 3D simulation is also carried out for a wavy wall of amplitude 0.5 and the results are compared. In fig. 3.12, streamwise mean velocity profiles are plotted at $X = 16.875$, $X = 31.875$, and $X = 46.875$ for 2D and 3D results. From fig. 3.12, it can be noted that both the cases give almost same result with a small variation near the wall for $X = 46.875$ location, which can be neglected. This type of agreement between 2D and 3D is also shown by Hnaien et al. [38] for dual jet and Benkehlifa et al. [15] for the plane wall jet. That is why, it is decided to go with 2D simulation to save computational time. From now onwards, only 2D results will be discussed further.

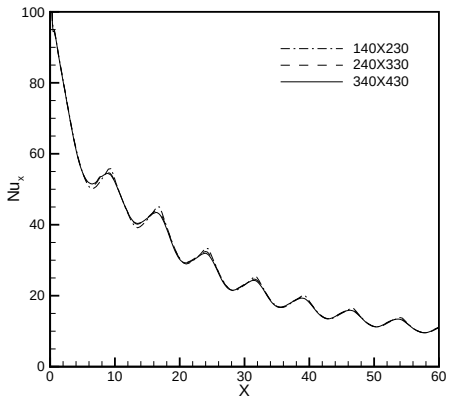

Figure 3.13: Local Nusselt number at the wall for amplitude 0.4

3.2.5 Grid independence test

3.2.5.1 Isothermal wavy wall

The computational domain is made of structural quadrilateral elements. Grid independence test is done for all the cases by increasing the number of elements in the longitudinal as well as in the lateral direction. It is made sure that the first grid near the wall should be inside the viscous sublayer by keeping y^+ and x^+ value less than 1. Fig. 3.13 shows the variation of local Nusselt number of the wavy wall with 0.4 amplitude. Three sets of grid of different sizes, viz. coarse grid (230×140), medium grid (330×240) and fine grid (430×340) are tested for the grid sensitivity. From fig. 3.13, it can be clearly seen that the coarse grid overpredicts the result for the maxima of the local Nusselt number and under predicts for the minima. As the number of grids increases from medium (330×240) to fine grid (430×340), no visible improvement is noticed. Hence, grid size 330×240 with 79200 elements is considered further for all the computational simulations.

3.2.5.2 Isothermal Modified wavy wall

In the case of modified wavy wall case, grid distribution is similar to the wavy wall as mentioned in the above section. Y^+ and X^+ are also remain less than 1 near the wall. The grid density has been varied as 230×140, 330×240 and 430×340 for the grid independence test similar to the isothermal wavy wall case. The variation of local Nusselt number along the partial wavy wall for 40% wavy wall is shown in fig. 3.14 for the three grid densities. There is no difference in the result of the later two denser grids whereas a little deviation is noticed at the crest and trough regions for the coarse grid (230×140). For solving the present problem, the grid with a density of 330×240 has been used to save the computational time.

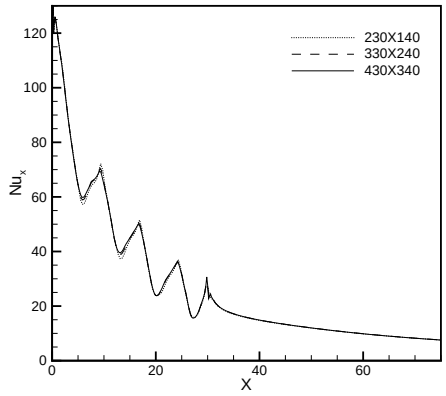

Figure 3.14: Variation of local Nusselt number along the wall for 40% wavy wall case

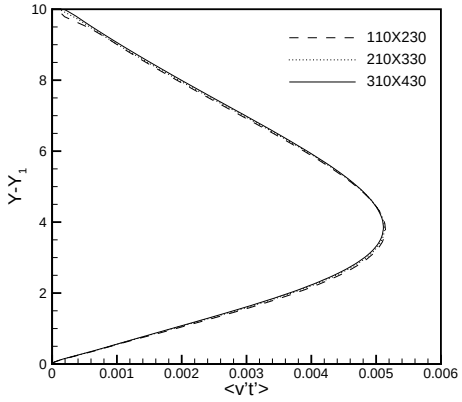

Figure 3.15: The variation of cross-stream turbulent heat flux at $X = 26.125$ for wavy wall of 0.4 amplitude

3.2.5.3 Adiabatic wavy wall

For performing grid independency test for adiabatic wavy wall, simulation has been performed on three different grid densities, coarse grid 110×230, medium grid210×330 and fine grid310×430. The numeric value before the $\times$ sign indicates the number of grid in cross-stream direction and the numeric value after the $\times$ sign indicates the number of grid in the streamwise direction. The fig. 3.15 shows the variation of cross-stream turbulent heat flux at the location $X = 26.125$ for different grid densities. The coarse grid result slightly over-predicts in the wall region and under-predicts in the outer region where as the medium grid210×330 and fine grid310×430 give almost same result. So, to optimise the time, medium grid 210×330 has been used to conduct the numerical simulation.

3.2.6 Selection of turbulent model

The numerical results of the present problem are compared with the results obtained from the experimental setup for two low Reynolds number models, viz. $k-\varepsilon$ RNG and $k-\omega$ SST, in order to decide the best suited model for the detailed numerical study. For comparision, the boundary conditions for the numerical simulation is kept same as the experimental condition, i.e. the bottom wall is adabatic. Fig. 3.16 shows the comparison of temperature obtained from the experimental result with the numerical result. The temperature profiles are compared for the amplitudes 0.2, 0.4 and 0.6, at three locations $X = 1.875$ (1st crest), $X = 39.375$ (6th crest) and $X = 58.125$ (8th trough). The outer scaling has been used to normalize the temperature and the distance normal to the wall. The difference in temperature between the specified point and the ambient is normalized by the difference in maximum temperature obtained at a particular location X and the ambient, i.e $\theta/\theta_{max} = (T - T_\infty)/(T_{max} - T_\infty)$. The distance normal to the wall $(Y - Y_1)$ is normalized by $Y_{T0.5}$, which is defined as the distance where θ becomes half of the θ_{max}. In the figure, it can be seen that for most of the cases, the result of RNG model matches very well with the experimental result. In the case of 0.2 amplitude, at the locations $X = 39.375$ and $X = 58.125$, the results of RNG model are little over-predicated with a maximum difference of 12% and 10% in the free jet region. The SST model over-predicts the temperature profile in the outer shear layer of jet in almost all the cases. The decay of wall temperature, $\theta_W = (T_W - T_\infty)/(T_0 - T_\infty)$ for 0.2 amplitude is compared in fig. 3.17a, where the numerical result matches very well with the experimental result near the exit of jet $X \leq 1.875$, and the numerical values start over-predicting as the fluid moves forward in the transition zone. In the experimental result, there is a sharp decay in the wall temperature. The difference in results reduces in the developed zone. Overall, RNG model works quite well for the wall temperature, with a maximum difference of 24.2% and 14.5% in the transition and developed zones respectively. The difference in the experimental and numerical values are due to the heat loss which is always present in the experimental study and can not be accounted for in the numerical simulation. Moreover, a uniform inlet jet velocity and temperature are considered as the input to the numerical simulation while it is not exactly flat near the edges in the experimental observations (figure 3.7a). Fig. 3.17b shows the variation of jet thermal half width for both the cases (experimental and numerical) for the case of wavy wall with 0.2 amplitude. For this case also, the RNG model gives a good agreement with the experimental results till $X = 43.125$, and as fluid moves further, the RNG results start getting deviated from the experimental results. A maximum difference of 24% and 36.5% in the results of RNG and SST models respectively, is noticed in the far field. From these discussions, it is clear that the RNG model performs well for the case of a turbulent

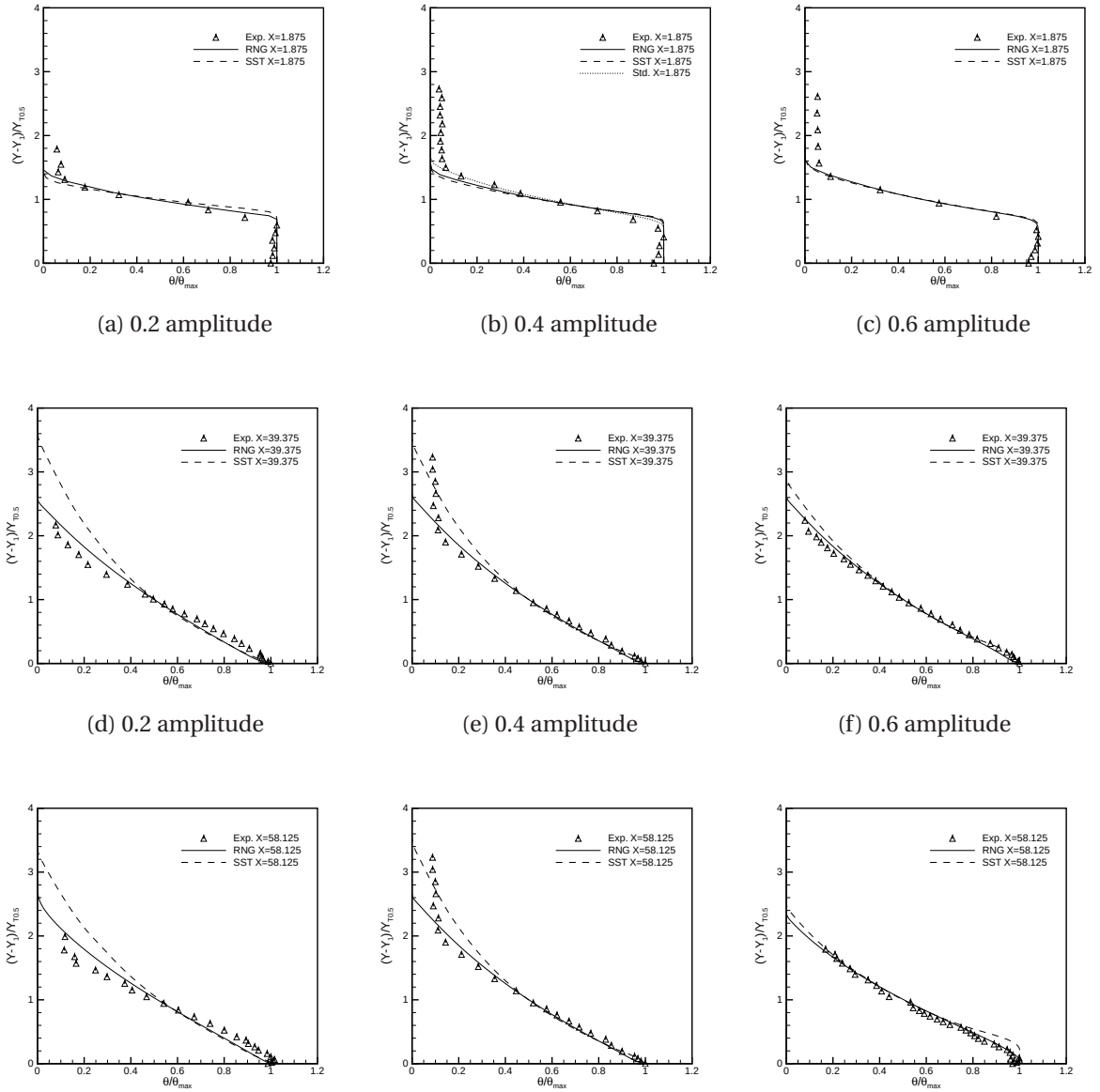

(a) 0.2 amplitude (b) 0.4 amplitude (c) 0.6 amplitude

(d) 0.2 amplitude (e) 0.4 amplitude (f) 0.6 amplitude

(g) 0.2 amplitude (h) 0.4 amplitude (i) 0.6 amplitude

Figure 3.16: The experimental and numerical results of streamwise mean velocity profile normal to the wall for different amplitudes

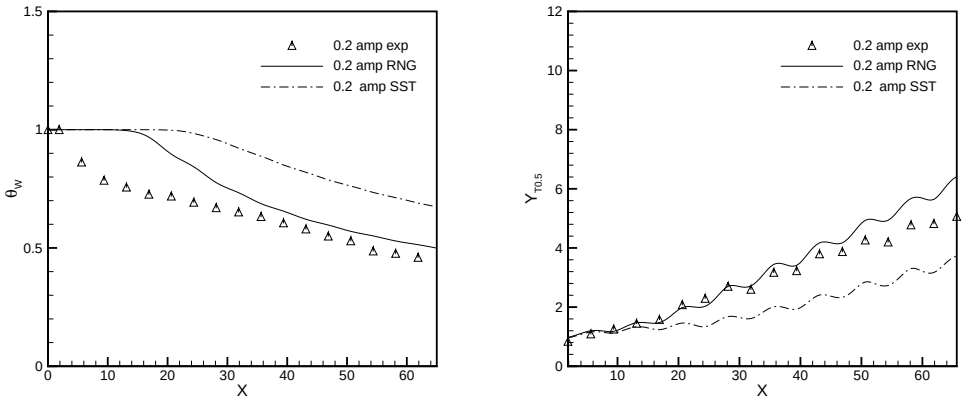

(a) (b)

Figure 3.17: The experimental and numerical results of (a) bottom wall temperature and (b) the growth of the thermal jet half width along the flow, for amplitude 0.2

wall jet flowing over a wavy wall. In the literature, many researchers [20, 24, 45, 104] have also noticed that the RNG model gives better agreement with the experimental results in comparison to other RANS models. So, RNG model has been selected for the further numerical simulation.

3.2.7 Code validation

Due to unavailability of experimental result for wavy wall jet, the numerical result is validated with the results of plane wall jet. The numerical approach used in the present research is validated with the results of Rostamy et al. [82], Naqavi et al. [67], Eriksson et al. [25], Holland and Liburdy [41] and AbdulNour et al. [1]. Rostamy et al. [82] have experimentally investigated the plane wall jet with a Reynolds number of 7500, to study the fluid flow characteristics. Fig. 3.18 shows the comparison of Reynolds shear stress profile normal to the wall at a location $X = 30$ with Rostamy et al. [82]. From fig. 3.18, it can be seen clearly that the present result best matches with the result of Rostamy et al. [82]. Naqavi et al. [67] have used DNS to study the heat and fluid flow characteristics of a turbulent wall jet with a heated isothemal wall for the Reynolds number of 7500. Fig 3.19 shows the comparison of the local maximum streamwise velocity (U_{max}) along the flow with the result of Naqavi et al. [67]. In fig. 3.19, the present result is in very good agreement with the literature result. In order to validate the thermal parameter, the normalized temperature ($\theta = (T - T_\infty)/(T_w - T_\infty)$) profile normal to the wall is compared with the result of Naqavi et al. [67] at the position $X = 35$, as shown in fig. 3.20. The present numerical result matches

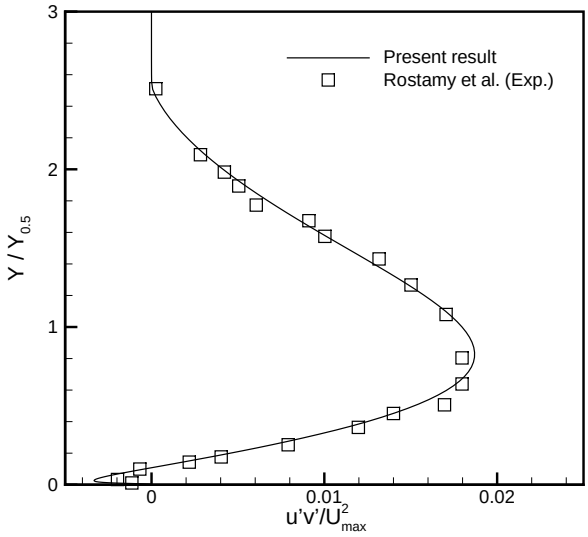

Figure 3.18: The variation of Reynolds shear stress in wall normal direction at the location $X = 30$

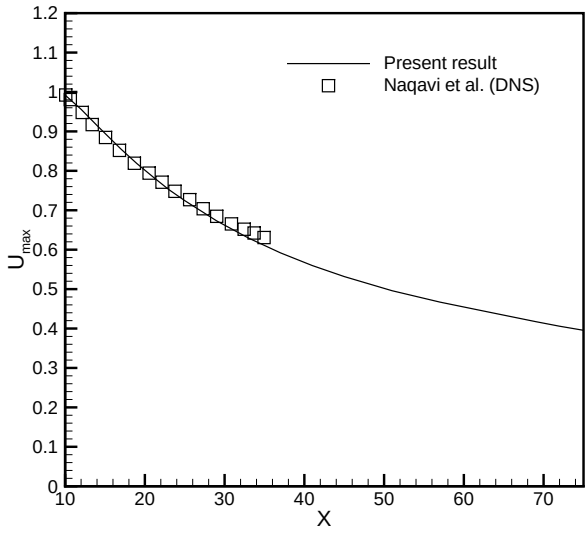

Figure 3.19: The variation of local maximum streamwise velocity along the flow for plane wall jet

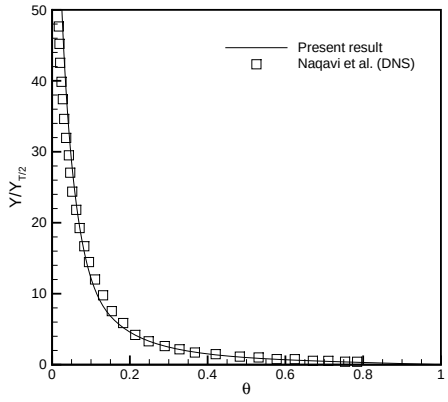

Figure 3.20: Normalized temperature profile normal to the wall at $X = 35$

very well with the result of Naqavi et al. [67] in near the wall region. The present result is in a very good agreement with the result of Naqavi et al. [67] for the temperature profile as well. To validate the turbulent parameter, the turbulent kinetic energy of the present problem has been compared with the result of Eriksson et al. [25]. The Reynolds number is kept at 9600 at the inlet, same as the value considered by Eriksson et al. [25]. In fig. 3.21, the validation of TKE is shown at the locations $X = 40$ and $X = 70$ in the transverse direction with the results of Eriksson et al. [25] and a very nice match can be seen between the literature results and the present results. For the validation of temperature profile, all the thermal and flow boundary conditions are taken similar to the Holland and Liburdy [41]. The Reynolds number is taken as 15000, the bottom wall is provided adiabatic condition and the vertical wall is maintained at a constant temperature equal to T_∞. Fig. 3.22 shows the decreasing curve of wall temperature along the flow for all the models and experimental data. The numerical result gives reasonable agreement in near flow field and they overpredicts in the far field. For the adiabatic wall, Joo and Durbin [48] and Holloway and Leylek [42] have also noticed significant difference in experimental and numerical results using RANS model. The main reason for difference in experimental and numerical results is the loss from the bottom wall, which is not accounted accurately in the numerical modelling. Figs. 3.23a, 3.23b, 3.23c, and 3.23d show the validation of temperature profile in the transverse direction for the locations $X = 10.4$, $X = 15.4$, $X = 20.3$ and $X = 25.2$, respectively. In the near field region, $X = 10.4$ and $X = 15.4$, the numerical results match very well with the experimental data with a little deviation in near wall region. Also, at the locations $X = 20.3$ and $X = 25.2$, the numerical results are in good agreement with the experimental data.

In the process of validation of heat transfer quantity, convection heat transfer coeffi-

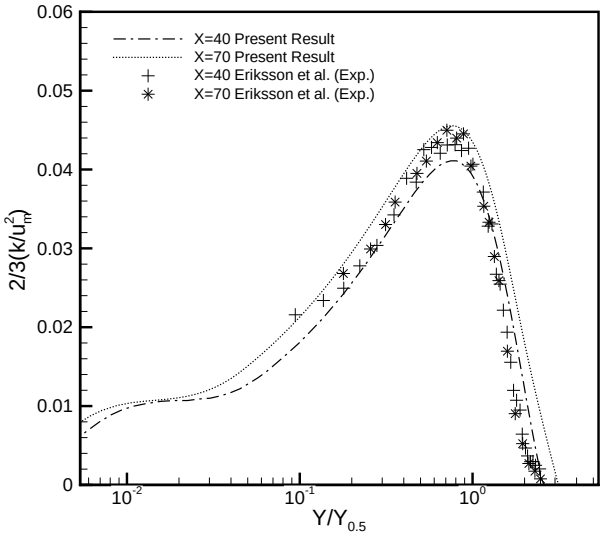

Figure 3.21: The variation of TKE at a location $X = 40$ and $X = 70$ in the transverse direction for a plane wall jet

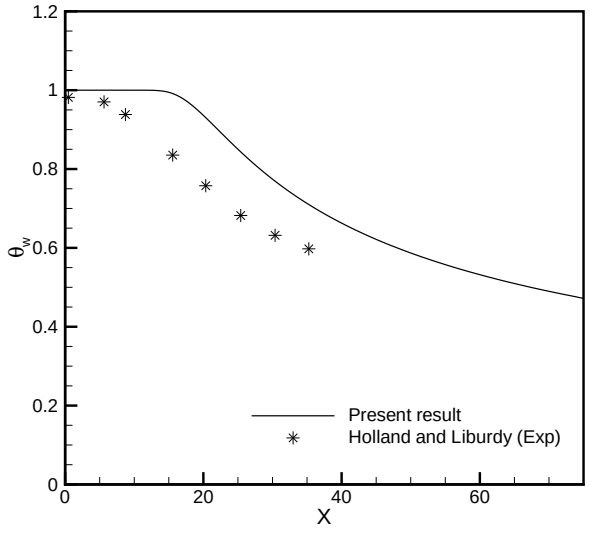

Figure 3.22: Normalized temperature variation of plate

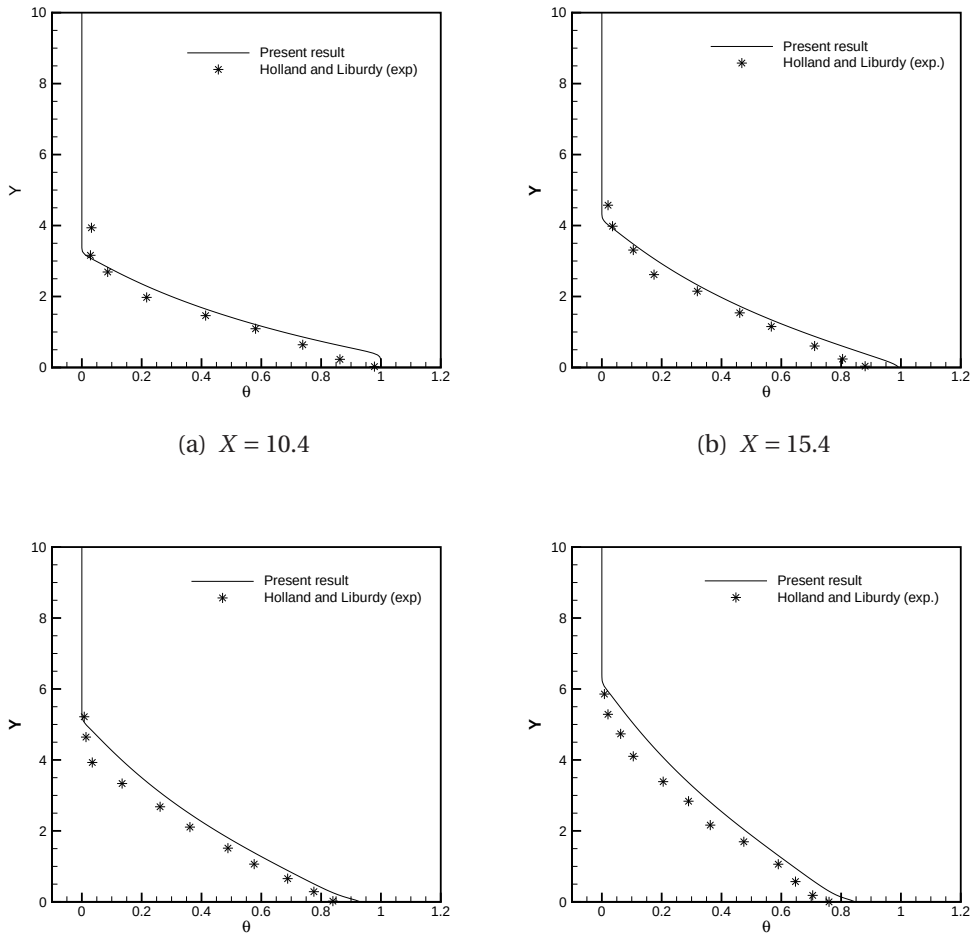

(a) $X = 10.4$

(b) $X = 15.4$

(c) $X = 20.3$

(d) $X = 25.2$

Figure 3.23: Nomarlised spanwise temperature profile at different locations of plane wall jet.

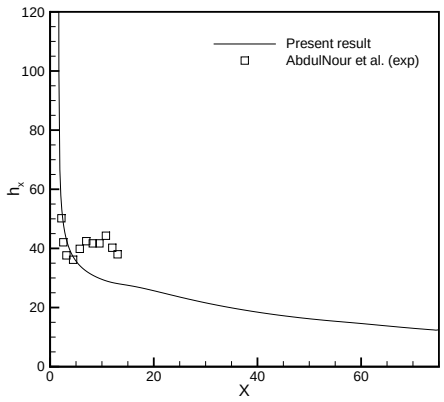

Figure 3.24: Comparison of convection heat transfer coefficient along the wall

cient along the wall is validated with the experimental result of AbdulNour et al. [1] in fig. 3.24. For validation, the boundary condition of AbdulNour et al. [1] (Reynolds number 7700) is considered, i.e. the bottom wall is in isothermal condition at 45řC and the jet is at ambient temperature of 22 řC. For convection heat transfer coefficient, Realizable and RNG give almost similar result and agrees well with the experimental data in near flow field region till $X < 5$; beyond this, deviation starts in the downstream direction. Still, RNG model results are closer to the experimental result in comparison to the Realizable and SST models. The maximum deviation between the experimental and the present result is 30.3% for RNG model. AbdulNour et al. [1] have reported the uncertainty in measuring convective heat transfer coefficient as 11% for the isothermal boundary condition case. This is one of the reasons for difference noticed in the results. They have also noticed the elevation in temperature of stagnant air inside the domain from $X = 8.26$ onwards, as the velocity profile does not goes to zero for larger Y. The alteration in the surrounding condition during the course of experiment, due to transfer of heat energy to the stagnant surrounding air, leads to difference in the result of numerical analysis from the experimental result. The experimental domain length is 1.5a (thermally inactive)+12.7a (thermally active), which is comparatively smaller than the present domain, i.e. 75a. The above-mentioned reasons are responsible for the difference in the experimental and numerical results. It must be noted here that the data of AbdulNour et al. [1] has been taken for validation due to unavailability of experimental data for heat transfer in the literature.